PHYSICAL REVIEW A **72**, 022717 (2005)

Energy of the quasifree electron in argon and krypton

C. M. Evans[1,*] and G. L. Findley[2,†]
[1]*Department of Chemistry and Biochemistry, Queens College–CUNY, Flushing, New York 11367, USA and Department of Chemistry, Graduate Center–CUNY, New York, New York 10016, USA*
[2]*Department of Chemistry, University of Louisiana at Monroe, Monroe, Louisiana 71209, USA*

(Received 6 March 2005; published 18 August 2005)

Field ionization measurements of CH_3I and C_2H_5I dopant high-n molecular Rydberg states in argon and krypton perturbers are presented as a function of perturber number density along various isotherms up to the density of the triple point liquid. Using these data, a new local Wigner-Seitz model for the density-dependent energy $V_0(\rho_P)$ of a quasifree electron in argon and krypton is developed. This model, which contains only one adjustable parameter, uses a local Wigner-Seitz radius derived from the local number density rather than from the bulk number density, includes a statistical mechanical calculation of both the ion/medium polarization energy and the electron/medium polarization energy, and includes the thermal kinetic energy of the quasifree electron. Using this model, $V_0(\rho_P)$ and the perturber-induced energy shift of the dopant ionization potential $\Delta_D(\rho_P)$ are calculated to within ±0.1% of experiment. Previously reported $V_0(\rho_P)$ data for xenon are also shown to be interpretable within this new model.

DOI: 10.1103/PhysRevA.72.022717 PACS number(s): 34.30.+h, 33.15.Ry, 31.70.Dk

I. INTRODUCTION

The study of the density-dependent behavior of a free electron in gases and liquids is important in many areas of chemistry, including the investigation of electron/perturber interactions in disordered systems. For example, since the electron mobility in a solvent (perturber P) is directly related to the energy minimum of a free electron $V_0(\rho_P)$ in the solvent of number density ρ_P [1–11], one can use $V_0(\rho_P)$ to study electron mobility effects of perturber parameters (e.g., molecular shape, strength of interaction, etc.). Electron mobility, in turn, can influence the kinetics of chemical reactions [12,13], especially electrochemical reactions. Thus, the ability to model $V_0(\rho_P)$ accurately has applications in the optimization of the choice of solvents and thermodynamic conditions for chemical reactions.

At low perturber number density, a perturber atom or molecule acts on a dopant Rydberg state by shifting the Rydberg state energy and by broadening the transition line shape as a result of collisional interactions. The perturber-induced shift of high-n Rydberg states can be explained within a simple model [14]. This model assumes that, due to the large size of the Rydberg state, the perturbers interact separately with the Rydberg electron and with the ionic core. Within this assumption, the shift of high-n Rydberg states, or of the dopant ionization energy, arises from two independent phenomena, namely the scattering of the Rydberg electron off of the perturber and the polarization of the perturber due to the ionic core. In other words [14],

$$\Delta_D(\rho_P) = \Delta_{sc}(\rho_P) + \Delta_{pol}(\rho_P), \tag{1}$$

where $\Delta_D(\rho_P)$ is the total shift in dopant ionization energy [i.e., $\Delta_D(\rho_P) = I(\rho_P) - I_g$, where $I(\rho_P)$ is the perturbed dopant ionization energy and I_g is the gas-phase ionization energy of the dopant], $\Delta_{sc}(\rho_P)$ is the "scattering" shift, $\Delta_{pol}(\rho_P)$ is the "polarization" shift, and ρ_P is the perturber number density.

For large n, the optical electron is loosely bound and can therefore be assumed to be nearly free. Moreover, near threshold the kinetic energy of the electron is approximately zero, so the scattering of the Rydberg electron by a perturber can be taken to be predominantly s-wave. In this case, $\Delta_{sc}(\rho_P)$ is given by [14]

$$\Delta_{sc}(\rho_P) = \frac{2\pi\hbar^2}{m} A \ \rho_P, \tag{2}$$

where m is the electron mass, A is the electron scattering length in the perturber medium (which may be either positive or negative depending on the nature of the perturber), and $\hbar$ is the reduced Planck constant. The shift due to the polarization of the perturbing molecules by the ionic core can be determined using [15–20]

$$\Delta_{pol}(\rho_P) = -10.78\left(\frac{1}{2}\alpha_P e^2\right)^{2/3} (\hbar \mathrm{v})^{1/3} \rho_P. \tag{3}$$

In this equation, α_P is the perturber polarizability, e is the electron charge, and v is the relative thermal velocity of the dopant and perturber molecules. Since $\Delta_{pol}(\rho_P)$ can be calculated and $\Delta_D(\rho_P)$ obtained experimentally, Eq. (1) has been used to determine the zero-kinetic-energy electron scattering length of various perturber atoms and molecules [17–21], including several fluorinated hydrocarbons [21]. Low-to-medium number density studies have also yielded insights into cluster formation [21]. However, the dopant/perturber interaction mechanisms developed in low-density studies do not extend into the high-density regime [11,16,17,22–24].

As ρ_P increases, Eq. (1) goes over smoothly to

---

[*] Email address: cevans@forbin.qc.edu

[†] Email address: findley@ulm.edu

$$\Delta_D(\rho_P) = V_0(\rho_P) + P_+(\rho_P), \tag{4}$$

where $\Delta_D(\rho_P)$ again is the total shift in dopant ionization energy, $V_0(\rho_P)$ is the quasifree electron energy in the host medium (i.e., the energy of the bottom of the conduction band of the perturber), and $P_+(\rho_P)$ is the average ion/medium polarization energy. Unfortunately, high-*n* Rydberg states in such high-density systems cannot be investigated using absorption spectroscopy or standard photoionization spectroscopy because of pressure broadening of the bound and autoionizing Rydberg states. With this limitation in mind, several groups have investigated very dense media using photoconductivity techniques [3–5,11,24–30]. Most recently, Reininger *et al.* [11,23,24,31–38] have exploited field ionization of high-*n* dopant Rydberg states as a method for determining the quasifree electron energy $V_0(\rho_P)$ in various atomic perturbers.

In this paper, we first outline previous experimental techniques used to obtain $V_0(\rho_P)$ from Eq. (4). We then discuss the original Wigner-Seitz model for $V_0(\rho_P)$ and give a brief history of subsequent modifications to this model. After discussing the experimental methods employed by us, we present new field ionization data for CH_3I and C_2H_5I in dense Ar and Kr, and we provide a statistical mechanical model to calculate $P_+(\rho_P)$ in Eq. (4) in order to determine $V_0(\rho_P)$ experimentally. Finally, we introduce a new local Wigner-Seitz theory that accurately models $V_0(\rho_P)$ over the entire density range and allows one to calculate $\Delta_D(\rho_P)$ to within ±0.1% of experiment. The results of this new theory are further tested by comparing known experimental measurements of $V_0(\rho_P)$ in Xe with our model calculations.

II. EXPERIMENTAL DETERMINATION OF V_0

The direct approach to obtaining $V_0(\rho_P)$ involves photoinjecting an electron from a metal into a dense perturber. Since $V_0(\rho_P)$ is the energy required to take an electron from a vacuum into the bulk fluid, the difference between the work function of the metal in a vacuum and in the fluid corresponds directly to $V_0(\rho_P)$. Thus, if the photoemission spectrum of a metal is measured in a vacuum and separately in the fluid, the difference in the threshold region can be used to determine $V_0(\rho_P)$. In Fig. 1, photoinjection data for Ar [6,11,24] and Kr [3,11,24] are shown. One clearly sees that there is considerable experimental scatter. Furthermore, the fitted curves through the experimental points do not extrapolate to zero energy in the absence of a perturber (i.e., in a vacuum). This problem results from the formation of oxide layers on the metal surface, which form a barrier through which a photoemitted electron must tunnel. Thus, the photoinjection energy of the oxide contaminated metal electrode is nonzero in the vacuum. A second problem is that the perturber interacts with the surface of the electrode and, thereby, changes the electronic structure of the electrode. This perturber/electrode interaction is dependent upon the surface area and roughness of the electrode, the type of metal, the nature of the perturber, and the number density of the perturber. Thus, modeling the perturber/electrode interaction is difficult, which makes the accurate correction of photoinjection data essentially impossible.

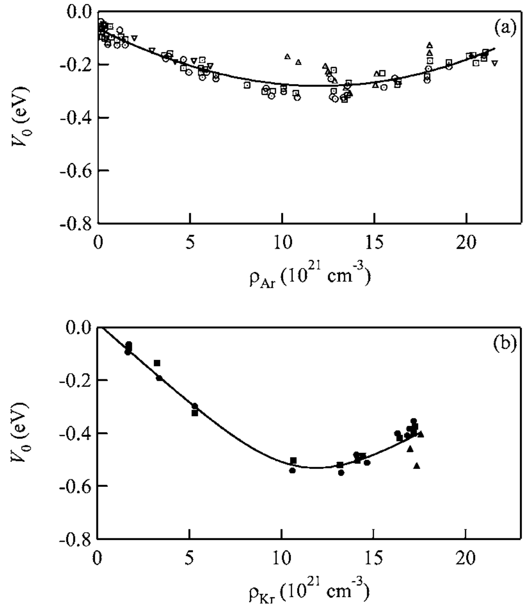

FIG. 1. $V_0(\rho_P)$ obtained from various photoinjection measurements, plotted as a function of perturber number density ρ_P. (a) P is Ar; (○) [6,11,24], (□) [6,11,24], (△) [11,24], and (▽) [11,24]. (b) P is Kr; (●) [3,11,24], (■) [3,11,24], and (▲) [11,24,30]. Lines provide a visual aid.

Since directly determining $V_0(\rho_P)$ using photoinjection is interpretationally problematic, Reininger and co-workers [11,23,24,31–38] developed an indirect method to obtain $V_0(\rho_P)$ experimentally. This method uses the relationship in Eq. (4) to extract $V_0(\rho_P)$ once one determines $\Delta_D(\rho_P)$ experimentally and calculates $P_+(\rho_P)$. Studies of atomic Rydberg states in the presence of a static electric field [39] show that high-*n* Rydberg states ionize at an electric field F_{cl} equal to $1/(16n^4)$, or that the change in the ionization energy is given by $I=-2F_{cl}^{1/2}$ (in atomic units). This process is referred to as classical field ionization. In the field ionization of molecular Rydberg states, vibrational and rotational effects must be taken into consideration, and these effects lead to the classical field-ionization limit being written as [24,39]

$$\Delta I = -c_0 F_{cl}^{1/2}, \tag{5}$$

where c_0 is a constant. A field ionization spectrum of a dopant in a dense medium is obtained by subtracting a photoionization spectrum measured at a low field F_L from a spectrum measured at a high field F_H after intensity normalization (necessary to remove the effects of secondary ionization [24]). The field ionization spectrum results from high-*n* Rydberg states that are field-ionized by F_H but not F_L. Variation in the strength of F_H leads to a shift in the energetic position of the field ionization peak. By plotting this shift as a function of the square root of the electric field, one can extrapolate the zero-field energy position of the ionization energy $I_0(\rho_P)$ using Eq. (5). Similarly, one can also correct for F_L by holding F_H constant and varying F_L. Thus, $\Delta_D(\rho_P)$ in Eq. (4) is obtained from

$$\Delta_{\mathrm{D}}(\rho_{\mathrm{P}}) = I_0(\rho_{\mathrm{P}}) - I_g \tag{6}$$

with $I_0(\rho_{\mathrm{P}})$ being determined experimentally from

$$I_0(\rho_{\mathrm{P}}) = I_{\mathrm{F}}(\rho_{\mathrm{P}}) + c_0(\sqrt{F_L} + \sqrt{F_H}), \tag{7}$$

where $I_{\mathrm{F}}(\rho_{\mathrm{P}})$ is the dopant ionization energy perturbed by the electric field and by the dense gas. Therefore, if one can calculate $P_+(\rho_{\mathrm{P}})$, one can determine $V_0(\rho_{\mathrm{P}})$ for a given perturber number density using Eqs. (4), (6), and (7).

The density-dependent average polarization energy $P_+(\rho_{\mathrm{P}})$ depends upon the position r_i of each of the N perturbers relative to the dopant at the moment of excitation. Reininger *et al.* [11,24,31–38] used a potential of the form

$$w_+(r_1, \ldots, r_{\mathrm{N}}) = -\frac{1}{2}\alpha_{\mathrm{P}} e^2 \sum_i^N r_i^{-4} f_+(r_i), \tag{8}$$

where $f_+(r)$ is a screening function that incorporates the repulsive interactions between the induced dipoles in the perturber medium. The screening function chosen was [24,31–38,40]

$$f_+(r) = 1 - \alpha_{\mathrm{P}} \pi \rho_{\mathrm{P}} \int_0^\infty \frac{1}{s^2} g_{\mathrm{PP}}(s) ds \times \int_{|r-s|}^{r+s} \frac{1}{t^2} f_+(t) g_{\mathrm{PD}}(t) \theta(r,s,t) dt, \tag{9}$$

where

$$\theta(r,s,t) = \frac{3}{2s^2}(s^2 + t^2 - r^2)(s^2 - t^2 + r^2) + (r^2 + t^2 - s^2), \tag{10}$$

and where the integration variables s and t represent the distance between the atom of interest and all other perturber atoms. In Eq. (9), $g_{\mathrm{PP}}(r)$ and $g_{\mathrm{PD}}(r)$ are the perturber/perturber and perturber/dopant radial distribution functions, respectively, where $g_{\mathrm{PD}}(r)$ reflects the distribution of perturber atoms around the ground-state dopant molecule. Using a canonical distribution, the probability of sampling a particular polarization energy W, then, is given by [24,31–38]

$$P(W) = \int \cdots \int \delta(W - w_+(r_1, \ldots, r_{\mathrm{N}})) \times \mathrm{e}^{-\beta U(r_1,\ldots,r_N)} \prod_i dr_i \Bigg/ \int \cdots \int \mathrm{e}^{-\beta U(r_1,\ldots,r_N)} \prod_i dr_i, \tag{11}$$

where $\beta = 1/(k_B T)$ (k_B is Boltzmann's constant) and $U(r_1, \ldots, r_N)$ is the multidimensional potential energy of the system prior to ionization. Assuming two-body spherically symmetric interactions, $U(r_1, \ldots, r_N)$ can be approximated by a sum of intermolecular pair potentials, or

$$U(r_1, \ldots, r_N) = \sum_{i=1}^N U_{\mathrm{PD}}(r_i) + \sum_{\substack{i,j=1 \\ i<j}}^N U_{\mathrm{PP}}(|r_i - r_j|), \tag{12}$$

where $U_{\mathrm{PD}}(r)$ and $U_{\mathrm{PP}}(r)$ are, respectively, the perturber/dopant and perturber/perturber intermolecular potentials. Reininger *et al.* [24,31–38] assumed Lennard-Jones 6-12 potentials for both $U_{\mathrm{PD}}(r)$ and $U_{\mathrm{PP}}(r)$ for all of the dopant/perturber systems studied. A moment analysis of the Fourier transform of Eq. (11) yields the first moment [24,31–38,41,42]

$$m_1 = -4\pi\rho_{\mathrm{P}} \int_0^\infty g_{\mathrm{PD}}(r) w_+(r) r^2 dr \tag{13}$$

after some (tedious) algebra. This moment represents the shift in the dopant ionization energy resulting from the average polarization of the perturber by the ionic core at the moment of excitation; or in other words, $P_+(\rho_{\mathrm{P}}) \equiv m_1(\rho_{\mathrm{P}})$.

Obviously, Eqs. (8)–(13) depend on the method used to calculate $g_{\mathrm{PP}}(r)$ and $g_{\mathrm{PD}}(r)$. For their calculations, Reininger *et al.* [24,31–38] chose a coupled homogeneous Percus-Yevick model [43],

$$\begin{aligned} g_{\mathrm{PD}}(r) &= r^{-1} \mathrm{e}^{-\beta U_{\mathrm{PD}}(r)} Y_{\mathrm{PD}}(r), \\ g_{\mathrm{PP}}(r) &= r^{-1} \mathrm{e}^{-\beta U_{\mathrm{PP}}(r)} Y_{\mathrm{PP}}(r), \end{aligned} \tag{14}$$

where

$$\begin{aligned} Y_{\mathrm{PD}}(r) &= \int_0^r dt \frac{dY_{\mathrm{PD}}(t)}{dt}, \\ Y_{\mathrm{PP}}(r) &= \int_0^r dt \frac{dY_{\mathrm{PP}}(t)}{dt}, \end{aligned} \tag{15}$$

with

$$\begin{aligned} \frac{d}{dr} Y_{\mathrm{PD}}(r) = 1 + 2\pi\rho_{\mathrm{P}} \int_0^\infty dt (\mathrm{e}^{-\beta U_{\mathrm{PD}}(t)} - 1) Y_{\mathrm{PD}}(t) &\times \Bigg[\mathrm{e}^{-\beta U_{\mathrm{PP}}(r+t)} Y_{\mathrm{PP}}(r+t) - \frac{r-t}{|r-t|} \mathrm{e}^{-\beta U_{\mathrm{PP}}(|r-t|)} \\ &\times Y_{\mathrm{PP}}(|r-t|) - 2t \Bigg], \\ \frac{d}{dr} Y_{\mathrm{PP}}(r) = 1 + 2\pi\rho_{\mathrm{P}} \int_0^\infty dt (\mathrm{e}^{-\beta U_{\mathrm{PP}}(t)} - 1) Y_{\mathrm{PP}}(t) &\times \Bigg[\mathrm{e}^{-\beta U_{\mathrm{PP}}(r+t)} Y_{\mathrm{PP}}(r+t) - \frac{r-t}{|r-t|} \mathrm{e}^{-\beta U_{\mathrm{PP}}(|r-t|)} \\ &\times Y_{\mathrm{PP}}(|r-t|) - 2t \Bigg]. \end{aligned} \tag{16}$$

Equations (14)–(16) are only valid when $\rho_{\mathrm{D}} \ll \rho_{\mathrm{P}}$. [Examples of the perturber/dopant and perturber/perturber radial distribution functions $g_{\mathrm{PP}}(r)$ and $g_{\mathrm{PD}}(r)$ determined from Eqs. (14)–(16) using a Lennard-Jones 6-12 potential for C_2H_5I in Ar are shown in Fig. 2].

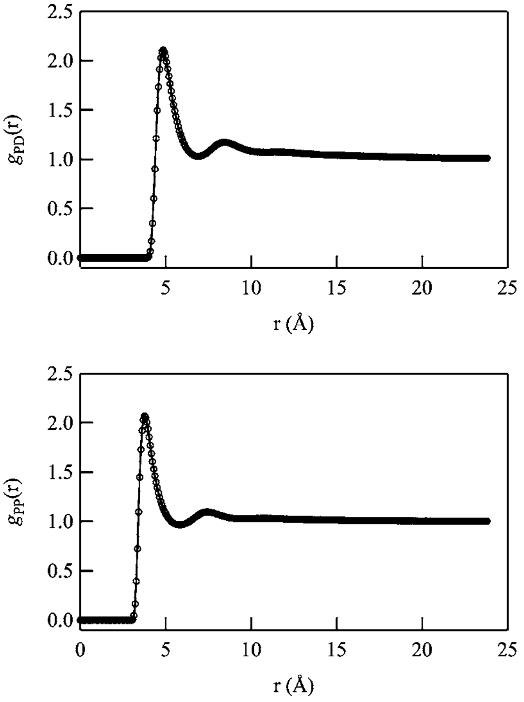

FIG. 2. Example perturber/dopant and perturber/perturber radial distribution functions $g_{PD}(r)$ and $g_{PP}(r)$, respectively, calculated using Eqs. (14)–(16), plotted as a function of distance from the central atom r. These RDF functions are for C_2H_5I/Ar and Ar/Ar at an Ar number density $\rho_{Ar}=8.00\times10^{21}$ cm^{-3}. The Lennard-Jones parameters used are $\sigma_{PP}=3.409$ Å, $\varepsilon_{PP}/k_B=119.5$ K, $\sigma_{PD}=4.394$ Å, and $\varepsilon_{PP}/k_B=138.1$ K. See text for discussion.

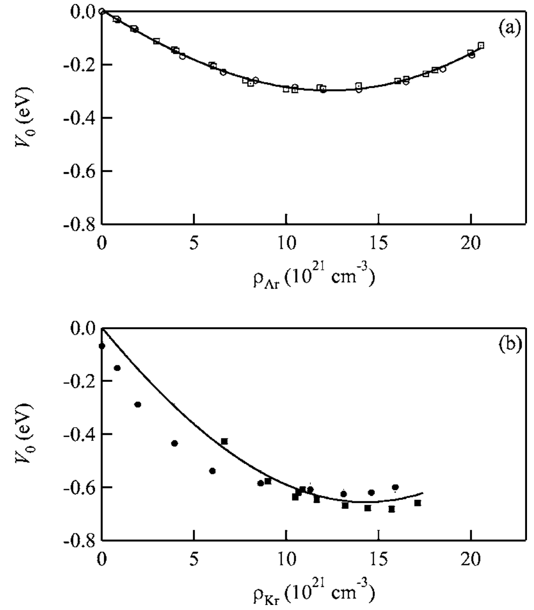

FIG. 3. $V_0(\rho_P)$ obtained from various field ionization measurements of dopant Rydberg states, plotted as a function of perturber number density ρ_P. (a) P is Ar; (○) D is CH_3I and (□) D is H_2S. (b) P is Kr; (●) D is CH_3I and (■) D is $(CH_3)_2S$. All data are taken from [11,24]. (——) represents a fit to experiment using $V_0(\rho_P) = a_0+a_1(\rho_P-a_2)+(a_3/a_4)\ln\{\cosh[a_4(\rho_P-a_2)]\}$ [1,6]. For (a) P is Ar [24], $a_0=-0.262$ eV, $a_1=0.0180\times10^{-21}$ eV cm^3, $a_2=16.4\times10^{21}$ cm^{-3}, $a_3=0.0905\times10^{-21}$ eV cm^3, and $a_4=0.0510\times10^{-21}$ cm^3. For (b) P is Kr [24], $a_0=-0.521$ eV, $a_1=0.0414\times10^{-21}$ eV cm^3, $a_2=19.3\times10^{21}$ cm^{-3}, $a_3=0.166\times10^{-21}$ eV cm^3, and $a_4=0.0480\times10^{-21}$ cm^3.

Reininger *et al.* [24,31–38] were able to obtain $V_0(\rho_P)$ from Eq. (4) using the experimental data for $\Delta_D(\rho_P)$, and $P_+(\rho_P)$ from Eq. (13). The results (cf. Fig. 3) were consonant with those obtained from photoinjection measurements (cf. Fig. 1). Thus, field ionization can be used to determine $V_0(\rho_P)$ experimentally without the complications present in photoinjection experiments. This permits one to test various theoretical calculations of $V_0(\rho_P)$ for accuracy across the entire density range.

III. THEORETICAL CALCULATION OF V_0

The first model of the behavior of V_0 started from the solution to the one-electron Schrödinger equation [44]

$$\left[-\frac{\hbar^2}{2m}\nabla^2+V(r)-E\right]\psi=0, \tag{17}$$

where $V(r)$ is the one-electron potential exerted by the neat fluid and E is the energy of the system. Unlike solids, where the symmetry of the potential is determined by the lattice structure, liquids have only an average symmetry. Therefore, most models assume that the potential is spherically symmetric about the perturber, and that the potential (neglecting fluctuations) has an average translational symmetry [7,8,10,11,24,44–51]

$$V(r)=V(r+2r_s), \tag{18}$$

where r_s is the Wigner-Seitz (WS) radius [44,52,53]

$$r_s=\sqrt[3]{\frac{3}{4\pi\,\rho_P}}. \tag{19}$$

The requirement that the first derivative of the wave function be continuous at the WS boundary leads to [7,8,10,11,24,44–51]

$$\left(\frac{\partial\psi_0}{\partial r}\right)\Bigg|_{r=r_s}=0. \tag{20}$$

Thus, V_0 is obtained by solving

$$\left[-\frac{\hbar^2}{2m}\nabla^2+V(r)\right]\psi_0\equiv V_0\psi_0 \tag{21}$$

under the boundary condition of Eq. (20). In the original model presented by Springett, Jortner, and Cohen (SJC) [44], the potential $V(r)$ was divided into two parts: $V_{\rm in}$, the potential due to the perturber inside the WS sphere, and $V_{\rm out}$, the contribution of all of the perturbers outside the sphere. $V_{\rm out}$ was approximated by its value in the center of the WS sphere, or [44]

$$V_{\rm out}=-\frac{3\alpha_P e^2}{2r_s^4}\left(1+\frac{8}{3}\pi\alpha_P\rho_P\right)^{-1}. \tag{22}$$

$V_{\rm in}$ was defined as the sum of an attractive polarization potential V_p and a repulsive atomic pseudopotential V_a. To evaluate V_p, the authors assumed that the electron distribution is uniform in the region $r_s/2 \leqslant r \leqslant r_s$, which led to [44]

$$V_p(r) = \int_{r_s/2}^{r_s} -\frac{\alpha_{\mathrm{P}} e^2}{2r^4} d^3r \Bigg/ \int_{r_s/2}^{r_s} d^3r = -\frac{12\alpha_{\mathrm{P}} e^2}{7r_s^4}, \qquad (23)$$

where the term $-\alpha_{\mathrm{P}} e^2/2r^4$ is the electron-induced dipole polarization potential. Equation (23) tends to underestimate the effect of $V_p(r)$ at low density and overestimates the effect at high density. However, this approximation does allow one to obtain an analytical solution for Eq. (21). The potential $V(r)$ in Eq. (21) can now be written [44]

$$V(r) = V_a(r) + U_p(\rho_{\mathrm{P}}), \qquad (24)$$

where $U_p(\rho_{\mathrm{P}})$ is a constant defined by

$$U_p(\rho_{\mathrm{P}}) = -\frac{3\alpha_{\mathrm{P}} e^2}{2r_s^4}\left[\frac{8}{7} + \left(1 + \frac{8}{3}\pi\ \alpha_{\mathrm{P}}\rho_{\mathrm{P}}\right)^{-1}\right]. \qquad (25)$$

By defining $V_a(r)$ as a simple hard-core potential [i.e., $V_a(r)=0$ for $r > r_h$ and $V_a(r)=\infty$ for $r < r_h$, where r_h is the hard-core radius], Eq. (21) becomes [44]

$$\left[-\frac{\hbar^2}{2m}\nabla^2 + U_p(\rho_{\mathrm{P}})\right]\psi_0 = V_0(\rho_{\mathrm{P}})\psi_0,$$

$$r_h < r < r_s, \qquad (26)$$

with the boundary conditions

$$\psi_0(r_h) = 0, \quad \left.\left(\frac{\partial\psi_0}{\partial r}\right)\right|_{r=r_s} = 0. \qquad (27)$$

Under these boundary conditions, Eq. (26) has the simple solution

$$\psi_0 = \frac{1}{r}\sin k_0(r - r_h), \qquad (28)$$

where

$$\tan k_0(r_s - r_h) = k_0 r_s. \qquad (29)$$

The value of $V_0(\rho_{\mathrm{P}})$, therefore, is given by [44]

$$V_0(\rho_{\mathrm{P}}) = E_k(\rho_{\mathrm{P}}) + U_p(\rho_{\mathrm{P}}), \quad E_k(\rho_{\mathrm{P}}) = \frac{(\hbar k_0)^2}{2m}. \qquad (30)$$

However, while the formalism in Eqs. (17)–(30) is easily computed, the comparison with experiment is not good, as is shown in Fig. 4.

Other calculations of $V_0(\rho_{\mathrm{P}})$ involving the Wigner-Seitz sphere differ only in the choice of potential [i.e., Eq. (24)]. For instance, Plenkiewicz *et al.* [45–50,54] used an atomic pseudopotential which more successfully reproduced the low-energy electron-atom scattering data in the gas phase, but underestimated $V_0(\rho_{\mathrm{P}})$ for high-density atomic fluids. However, the calculated values differed from the experimental values by a minimum of 0.05 eV. Iakubov *et al.* [9,55] also modified the SJC model by changing the pseudopotential. Their pseudopotential was based on known atomic parameters and the radial distribution function in the liquid. These calculations tended to overestimate $V_0(\rho_{\mathrm{P}})$ by 0.1–0.5 eV, representing an error of around 30%. Stampfli and Bennemann [52] improved the SJC model by avoiding the approximation used to calculate the central atom polarization potential [i.e., Eq. (25)]. Their calculations also allowed the hard-core radius of the repulsive pseudopotential V_a to be an adjustable parameter. However, since $U_p(\rho_{\mathrm{P}})$ is no longer a constant, Eq. (26) can only be solved numerically in their model. Moreover, this model underestimates $V_0(\rho_{\mathrm{P}})$ by a minimum of 0.01 eV (or 3%) for most of the density range. In the last several years, other theoretical techniques [56–62] such as path integral molecular dynamics (PIMD) [56–58], diffusion Monte Carlo (DMC) methods [61], the block Lanczos diagonalization (BLD) method [61], quantum molecular dynamics (QMD) [61], and a random-phase approximation within multiple-scattering theory [62] have been employed for the evaluation of $V_0(\rho_{\mathrm{P}})$ in rare-gas fluids. These methods all tend to have minimum errors within ±5–10 % of experiment. In general, the WS models are superior to other methods in terms of accuracy and simplicity. Figure 5 compares some of the V_0 calculation procedures for Ar and Kr with the experimental data and clearly illustrates that none of the current theoretical methods work across the entire density range.

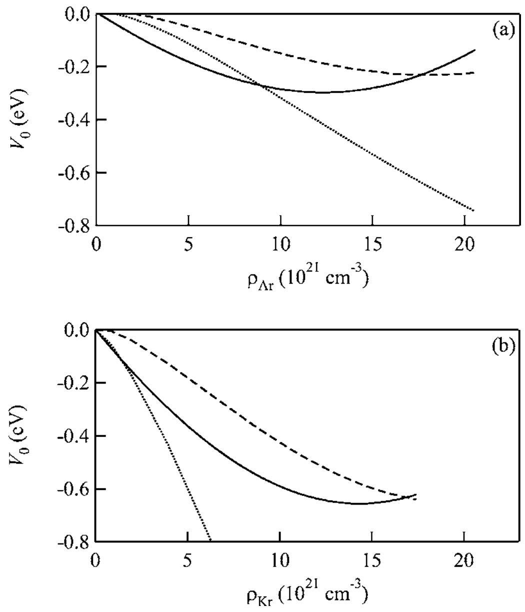

FIG. 4. Various $V_0(\rho_{\mathrm{P}})$ calculations [24,44] plotted as a function of perturber number density ρ_{P}. (a) P is Ar. (b) P is Kr. (——) is a nonlinear least-squares fit to the experimental data of Fig. 3 using an empirical function for $V_0(\rho_{\mathrm{P}})$ from [1]. (⋯⋯), $V_0(\rho_{\mathrm{P}})$ calculated using Eq. (30) with $r_h=|A|$ (i.e., $A=-0.82$ Å for Ar and $A=-1.60$ Å for Kr). (- - - -), $V_0(\rho_{\mathrm{P}})$ calculated using Eq. (30) with r_h adjusted to provide the best possible fit to experiment (i.e., $r_h=0.91$ Å for Ar and $r_h=1.04$ Å for Kr).

IV. EXPERIMENTAL PROCEDURES

Photoionization spectra were measured with monochromatized synchrotron radiation [21] having a resolution of 0.9 Å, or 8 meV in the spectral region of interest. This radiation

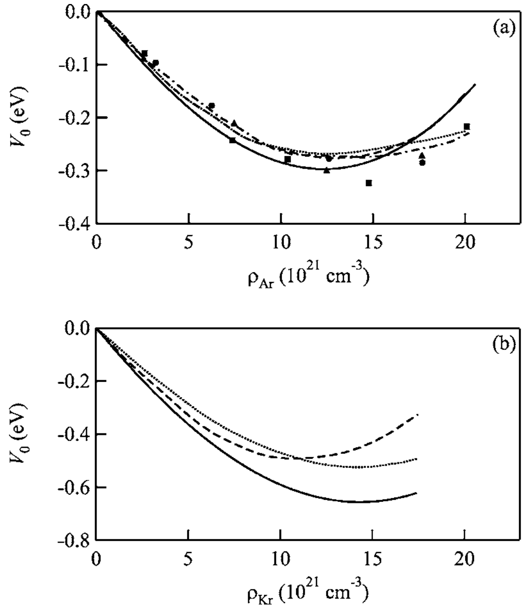

FIG. 5. Comparison of the experimentally determined conduction-band energy $V_0(\rho_P)$ plotted as a function of perturber number density ρ_P, represented by (——), to various calculated values. (a) P is Ar and (b) P is Kr. (——-) is a nonlinear least-squares fit to the experimental data of Fig. 3 using an empirical function for $V_0(\rho_P)$ from [1]. (· · · · ·) is calculated using more accurate pseudopotentials [49,50]. (---) is obtained by assuming that $U_p(\rho_P)$ is nonconstant and r_h is adjustable [51]. (-·-·-) is determined using a random-phase approximation within multiple scattering theory [62]. (●) and (▲) are calculated using quantum molecular dynamics [57], and (■) is determined using path integral molecular dynamics [58]. See text for discussion. This figure is adapted from [24].

entered a copper experimental cell [21], equipped with entrance and exit MgF_2 windows, that is capable of withstanding pressures of up to 100 bar. This cell, which possesses two parallel plate electrodes (stainless steel, 3 mm spacing) aligned perpendicular to the windows, was connected to an open flow cryostat and resistive heater system allowing the temperature to be controlled to within ±0.5 °C. The light path within the cell is 1.0 cm. The intensity of the synchrotron radiation exiting the monochromator was monitored by measuring the current across a Ni mesh intercepting the beam prior to the experimental cell. All photoionization spectra are normalized to this current.

The low field F_L and high field F_H necessary to obtain the best field ionization spectra are system-dependent and were determined by measuring field ionization spectra at various low fields and high fields for multiple perturber number densities. All data are energetically corrected for the effects of both the low field and high field using Eq. (7) with $c_0 = 4.3 \pm 0.1 \times 10^{-4}$ eV cm$^{1/2}$ V$^{-1/2}$ for CH_3I and $c_0 = 3.0 \pm 0.5 \times 10^{-4}$ eV cm$^{1/2}$ V$^{-1/2}$ for C_2H_5I. The energy uncertainty due to the low- and high-field correction was obtained by measuring the field ionization spectra of pure CH_3I and C_2H_5I at different low and high fields and was determined to be ±5 meV and ±6 meV, respectively, for CH_3I and C_2H_5I. The energy of a field ionization peak was found using a nonlinear least-squares analysis with a Gaussian fit function having a goodness of fit error determined within a 95% confidence level. The total error range for any experimental point, therefore, is given by a sum of the field correction error, the goodness of fit error, and the error arising from the energy uncertainty due to the resolution of the monochromator (i.e., ±4 meV). This total error averages to ±0.015 eV for the measurements involving CH_3I and to ±0.020 eV for the measurements involving C_2H_5I.

CH_3I (Aldrich, 99.45%), C_2H_5I (Sigma, 99.1%), argon (Matheson Gas Products, 99.9999%), and krypton (Matheson Gas Products, 99.998%) were used without further purification. Absorption spectra were measured for CH_3I (0.1 mbar) and C_2H_5I (0.5 mbar) to verify the absence of impurities. Absorption spectra of argon and krypton were measured at low number density and at high number density to check for the presence of trace impurities. No trace impurities were observed in argon. In krypton, however, we observed a small xenon impurity (<5 ppm from Matheson lot analysis). This impurity did not effect the determination of field ionization spectra for either dopant at any krypton number density. The number densities of both argon and krypton were calculated from the Strobridge equation of state [63] using a standard iterative technique. (The coefficients for the Strobridge equation of state for argon and krypton were obtained from Gosman *et al.* [64] and from Streett and Staveley [65], respectively.) The error in the number density calculated using the Strobridge equation of state was estimated to be ±0.2% of the density over the entire density range for both argon and krypton [64,65].

Both the gas handling system and the procedures employed to ensure homogeneous mixing of the dopant and perturber have been described previously [21]. The base pressure in the gas handling system was in the low 10^{-8} Torr range. In order to ensure no perturber contamination by the dopant, the gas handling system was allowed to return to the low 10^{-7} Torr range before the addition of the perturber. Cross contamination between dopant/pertuber systems was prevented by baking the gas handling system until the pressure was in the low 10^{-8} Torr range before introducing a new dopant/perturber system.

V. RESULTS AND DISCUSSION

While experimental data exist for the energy of a quasifree electron $V_0(\rho_P)$ in Ar and Kr (cf. Figs. 1 and 3), we chose to obtain new experimental data along isotherms in order to evaluate temperature effects. Figure 6 presents the perturber induced shift of the dopant ionization energy $\Delta_{D,EXP}(\rho_P)$ of CH_3I (solid markers) and C_2H_5I (open markers) in dense Ar and Kr plotted as a function of perturber number density ρ_P. The data in Fig. 6(a) (i.e., P is Ar) were taken along the noncritical isotherms -114.8 ± 0.6 °C and -117.6 ± 0.7 °C as well as at various other noncritical temperatures for the higher densities (since at $T < T_c$, the density does not vary much over the pressure range of 0–80 bar along any given isotherm). Similarly, the data in Fig. 6(b) were obtained along the noncritical isotherms -57.1 ± 0.9 °C and -60.0 ± 0.5 °C as well as at other temperatures for the higher densities.

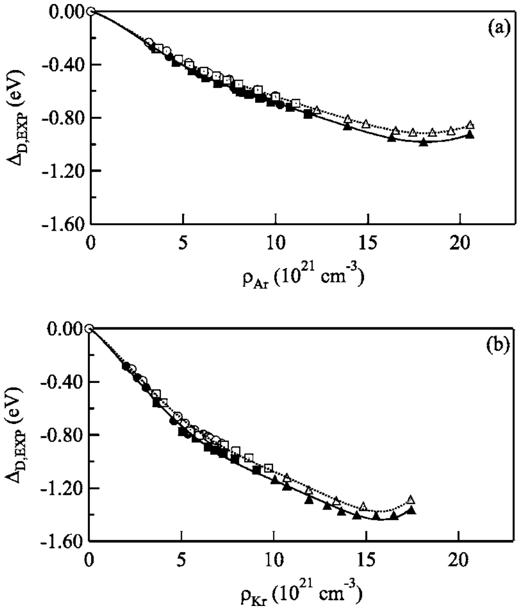

FIG. 6. The experimental perturber-induced shift of dopant ionization energies $\Delta_{D,EXP}(\rho_P)$ plotted as a function of perturber number density ρ_P. (a) P is Ar at (●, ○) −114.8 °C, at (■, □) −117.6 °C, and at (▲, △) various other noncritical temperatures. (b) P is Kr at (●, ○) −57.1 °C, at (■, □) −60.0 °C, and at (▲, △) various other noncritical temperatures. Solid markers represent D $=CH_3I$, and open markers represent $D=C_2H_5I$. The lines are a nonlinear least-squares fit to experiment using a seventh-order polynomial function and are provided as a visual aid. See text for discussion.

In order to determine $V_0(\rho_P)$ experimentally from Eq. (4), the average ion/perturber polarization energy $P_+(\rho_P)$ must be obtained. We chose to calculate $P_+(\rho_P)$ using Eqs. (8)–(13) with the radial distribution functions determined from Eqs. (14)–(16) and the intermolecular potentials given by [66]

$$U_{ij}(r) = 4\varepsilon_{ij}\left[\left(\frac{\sigma_{ij}}{r}\right)^{12} - \left(\frac{\sigma_{ij}}{r}\right)^{6}\right] - \frac{1}{r^6}(\alpha_i\mu_j^2 + \alpha_j\mu_i^2) + \frac{\mu_i\mu_j}{r^3}[\sin\theta_i \sin\theta_j \cos(\phi_i - \phi_j) - 2\cos\theta_i \cos\theta_j], \tag{31}$$

where ij is PP or PD. In this general form of Eq. (31), with indices omitted, ε and σ are the standard Lennard-Jones 6-12 potential parameters, α is the polarizability of the perturber or dopant, μ is the dipole moment of the perturber or dopant, and θ and ϕ are the angles of the perturber/perturber or perturber/dopant dipole moments oriented relative to local coordinates with coincident z axes. We chose Eq. (31) as the general intermolecular potential because of its applicability to a wide variety of dopant/perturber systems. For the case of the systems presented here, however, where the perturber is a rare gas but the dopant is a polar molecule, Eq. (31) simplifies to

TABLE I. Dopant and perturber thermodynamic information used to obtain Lennard-Jones potentials and to calculate radial distribution functions. α is the polarizability in Å^3, μ is the dipole moment in Debye, T_c is the critical temperature, and P_c is the critical pressure. All data are taken from *CRC Handbook of Chemistry and Physics*, 84th ed., edited by D. R. Lide (CRC Press, 2004).

	α(Å^3)	μ(D)	T_c(K)	P_c(bar)
Ar	1.6411	0	150.86	48.98
Kr	2.4844	0	209.46	55.20
CH_3I	7.97	1.641	528	65.9
C_2H_5I	10.0	1.976	554	47.0

$$U_{PP}(r) = 4\varepsilon_{PP}\left[\left(\frac{\sigma_{PP}}{r}\right)^{12} - \left(\frac{\sigma_{PP}}{r}\right)^{6}\right] \tag{32}$$

for the perturber/perturber interactions and

$$U_{PD}(r) = 4\varepsilon_{PD}\left[\left(\frac{\sigma_{PD}}{r}\right)^{12} - \left(\frac{\sigma_{PD}}{r}\right)^{6}\right] - \frac{1}{r^6}\alpha_P\mu_D^2 \tag{33}$$

for the dopant/perturber interactions. Equation (33) can be rearranged into standard Lennard-Jones form, namely

$$U_{PD}(r) = 4\varepsilon\left[\left(\frac{\sigma}{r}\right)^{12} - \left(\frac{\sigma}{r}\right)^{6}\right], \tag{34}$$

where [66]

$$\varepsilon \equiv \varepsilon_{PD}\left[1 + \frac{\alpha_P\mu_D^2}{4\varepsilon_{PD}\sigma_{PD}^6}\right]^2,$$

$$\sigma \equiv \sigma_{PD}\left[1 + \frac{\alpha_P\mu_D^2}{4\varepsilon_{PD}\sigma_{PD}^6}\right]^{-1/6}. \tag{35}$$

In order to obtain ε_{PD} and σ_{PD}, we used the Sikora combining rules [67] with ε_{DD} and σ_{DD} determined using the critical point data [68,69] for the various dopants. The information necessary to obtain the intermolecular potential parameters is given in Table I, and the intermolecular potential parameters used in all of the calculations presented here are given in Table II.

The average ion/perturber polarization energies $P_+(\rho_P)$ for CH_3I and C_2H_5I in Ar and in Kr, calculated from Eq. (13), are shown as a function of perturber number density ρ_P in Figs. 7(a) (P is Ar) and 7(b) (P is Kr). Subtracting $P_+(\rho_P)$ from $\Delta_D(\rho_P)$ leads to the experimental determination of $V_0(\rho_P)$, which is presented in Fig. 8 as a function of ρ_P. Clearly, the experimentally determined $V_0(\rho_P)$ in Fig. 8 is similar to that previously reported from earlier field ionization measurements (cf. Fig. 3) and from photoconduction measurements (cf. Fig. 1). The small differences between the data of Fig. 3 and those of Fig. 8 can be attributed to the change in the average ion/perturber polarization energies because of the choice of intermolecular potentials. The experimentally determined $V_0(\rho_P)$ also shows little to no temperature dependence along noncritical isotherms. The behavior along the critical isotherm around the critical point of the

TABLE II. Lennard-Jones parameters used in the radial distribution function calculations [i.e., Eqs. (14)–(16) of text] and average polarization energies [i.e., Eqs. (13) and (39) of text].

	σ_{ij}(Å)	ε_{ij}/k_B(K)	σ(Å)[a]	ε/k_B(K)[a]
Ar-Ar	3.409	119.5		
Kr-Kr	3.591	172.7		
CH_3I-CH_3I	4.761	402.4		
C_2H_5I-C_2H_5I	5.413	422.3		
CH_3I-Ar	4.081	158.8	4.074	162.2
C_2H_5I-Ar	4.402	135.1	4.394	139.1
CH_3I-Kr	4.173	214.1	4.166	218.6
C_2H_5I-Kr	4.495	187.8	4.487	191.8

[a] From Eq. (35) of text.

perturber is more complex and will be discussed in later publications [70–72].

As explained in more detail below, our theoretical treatment of $V_0(\rho_P)$ differs from the original SJC model in several significant ways. First, the translational symmetry for the system is defined by a local Wigner-Seitz radius determined from the perturber/perturber radial distribution function, not from the bulk Wigner-Seitz radius [i.e., Eq. (19)]. Second, the average electron/medium polarization is determined in a similar manner to the average ion/medium polarization shift [i.e., Eqs. (6)–(13)]. Third, since we have controlled the temperature to ±0.5 °C, we include the thermal energy of the quasifree electron (i.e., (3/2) k_BT, which is greater that the experimental error in these measurements). Finally, a phase-shift parameter is added to reflect the scattering of the quasifree electron off of the rare-gas atoms contained within the solvent shell.

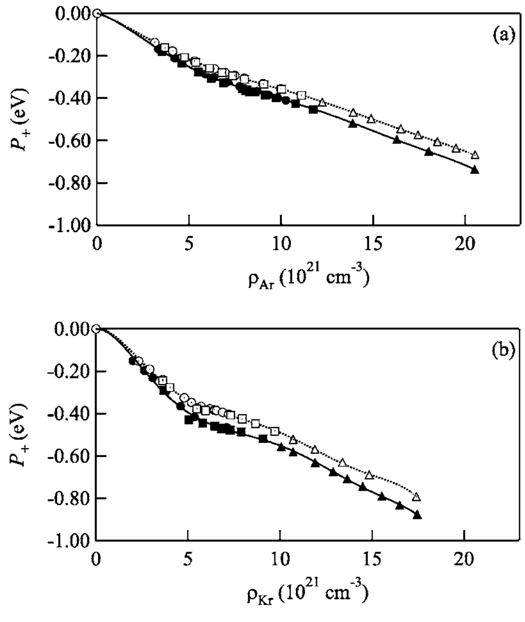

FIG. 7. The average ion/perturber polarization energy $P_+(\rho_P)$, calculated from Eq. (13) using the parameters in Table II, plotted as a function of perturber number density ρ_P. (a) P is Ar at (●, ○) −114.8 °C, at (■, □) −117.6 °C, and at (▲, △) various other noncritical temperatures. (b) P is Kr at (●, ○) −57.1 °C, at (■, □) −60.0 °C, and at (▲, △) various other noncritical temperatures. Solid markers represent D = CH_3I, and open markers represent D = C_2H_5I. The lines are a nonlinear least-squares fit to experiment using a seventh-order polynomial function and are provided as a visual aid. See text for discussion.

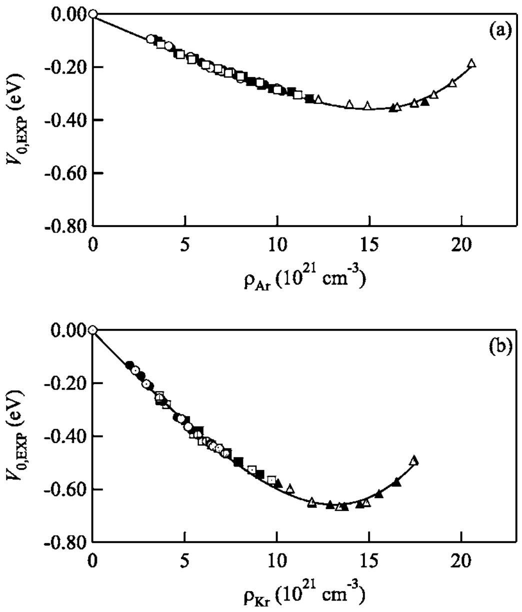

FIG. 8. $V_{0,EXP}(\rho_P)$, determined from Eq. (4) by subtracting $P_+(\rho_P)$ in Fig. 7 from the experimentally determined perturber-induced shift of dopant ionization energies $\Delta_{D,EXP}(\rho_P)$ in Fig. 6, plotted as a function of perturber number density ρ_P. (a) P is Ar at (●, ○) −114.8 °C, at (■, □) −117.6 °C, and at (▲, △) various other noncritical temperatures. (b) P is Kr at (●, ○) −57.1 °C, at (■, □) −60.0 °C, and at (▲, △) various other noncritical temperatures. Solid markers represent D = CH_3I and open markers represent D = C_2H_5I. (—) is a nonlinear least-squares fit to experiment using $V_0(\rho_P)=a_0+a_1(\rho_P-a_2)+(a_3/a_4)\ln\{\cosh[a_4(\rho_P-a_2)]\}$ [1,6]. For (a) P is Ar, $a_0=0.0347$ eV, $a_1=0.120\times10^{-21}$ eV cm^3, $a_2=22.9\times10^{21}$ cm^{-3}, $a_3=0.151\times10^{-21}$ eV cm^3, and $a_4=0.141\times10^{-21}$ cm^3. For (b) P is Kr, $a_0=0.0561$ eV, $a_1=0.192\times10^{-21}$ eV cm^3, $a_2=21.6\times10^{21}$ cm^{-3}, $a_3=0.270\times10^{-21}$ eV cm^3, and $a_4=0.106\times10^{-21}$ cm^3.

As is usual, our model begins with the one-electron Schrödinger equation [cf. Eq. (17)]. We also assume that the potential is spherically symmetric about the perturber and that the potential (neglecting fluctuations) has an average translational symmetry. However, we do not assume that the average distance between atoms in a gas can be determined by dividing the volume into spheres defined by the bulk number density [cf. Eq. (19)]. In dense gases, one does not have a uniform distribution of perturbers because of perturber/perturber interactions. Thus, the translational symmetry boundary condition must reflect this nonuniformity. One way to meet this requirement is to obtain the local number density from the radial distribution function, since [73,74]

$$\rho_P(r) = g_{PP}(r)\rho_P, \tag{36}$$

where $\rho_P(r)$ is the local perturber number density and ρ_P is the bulk perturber number density. In this case, then, the translational symmetry is defined by a local Wigner-Seitz radius

$$r_\ell = \sqrt[3]{\frac{3}{4\pi g_{\max}\rho_{\mathrm{P}}}}, \tag{37}$$

where $g_{\max}$ is the maximum of the radial distribution function. Thus $r_\ell < r_s$, because the local density at the first solvent sphere is larger than the bulk density. The local Wigner-Seitz radius, therefore, represents one-half the average spacing between rare-gas atoms in the first solvent shell, with the translation symmetry of the potential being given by

$$V(r) = V(r + 2r_\ell). \tag{38}$$

Like the SJC model [44], we assume that $V(r)$ is divided into two parts: an attractive electron/perturber polarization energy $P_-(\rho_{\mathrm{P}})$, which is similar to $U_p(\rho_{\mathrm{P}})$ in the SJC model [i.e., Eq. (25)], and a repulsive atomic pseudopotential $V_a(r)$.

We calculate the attractive electron/perturber polarization energy $P_-(\rho_{\mathrm{P}})$ in a manner similar to that of the ion polarization energy $P_+(\rho_{\mathrm{P}})$ in Eqs. (8)–(13). The interaction potential used is that originally proposed by Lekner [40],

$$w_-(r_1, \ldots, r_{\mathrm{N}}) = -\frac{1}{2}\alpha_{\mathrm{P}} e^2 \sum_i^N r_i^{-4} f_-(r_i), \tag{39}$$

where $f_-(r)$ is a screening function given by

$$f_-(r) = 1 - \alpha_{\mathrm{P}}\pi\rho_{\mathrm{P}} \int_0^\infty \frac{1}{s^2} g_{\mathrm{PP}}(s)\,ds \int_{|r-s|}^{r+s} \frac{1}{t^2} f_-(t)\,\theta(r,s,t)\,dt, \tag{40}$$

with $\theta(r,s,t)$ as defined in Eq. (10). The moment analysis of the probability distribution [i.e., Eq. (11)] yields the first moment

$$m_1 = -4\pi\rho_{\mathrm{P}} \int_0^\infty g_{\mathrm{PP}}(r) w_-(r) r^2 dr \equiv P_-(\rho_{\mathrm{P}}), \tag{41}$$

after some algebra. [Figure 9 shows the calculated average electron/perturber polarization energy $P_-(\rho_{\mathrm{P}})$ plotted as a function of ρ_{P} for both Ar and Kr.] Thus, the potential $V(r)$ in Eq. (21) becomes

$$V(r) = V_a(r) + P_-(\rho_{\mathrm{P}}), \tag{42}$$

where $P_-(\rho_{\mathrm{P}})$ is a constant for a fixed perturber number density. As in the SJC treatment, we define $V_a(r)$ as a hard-core potential [i.e., $V_a(r)=0$ for $r > r_h$ and $V_a(r)=\infty$ for $r < r_h$, where r_h is the hard core radius]. However, we set r_h equal to the absolute value of the scattering length A of the perturber. Thus, the one-electron Schrödinger equation becomes

$$\left[-\frac{\hbar^2}{2m}\nabla^2 + P_-(\rho_{\mathrm{P}})\right]\psi_0 = V_0\psi_0,$$

$$|A| < r < r_\ell, \tag{43}$$

with the boundary conditions

$$\psi_0(|A|) = 0, \qquad \left(\frac{\partial\psi_0}{\partial r}\right)\Bigg|_{r=r_\ell} = 0. \tag{44}$$

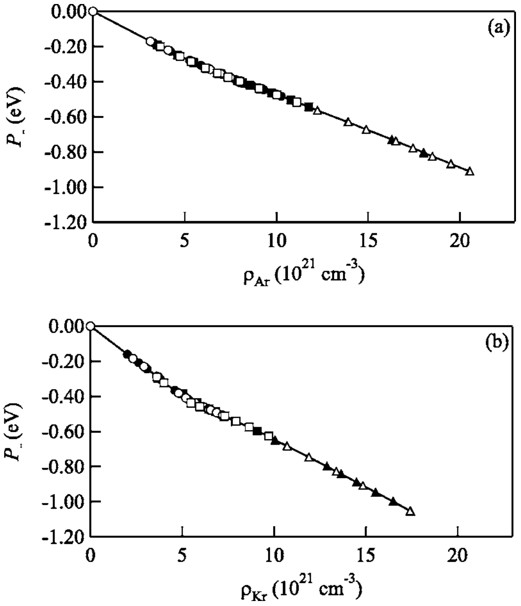

FIG. 9. The average electron/perturber polarization energy $P_-(\rho_{\mathrm{P}})$, calculated from Eq. (39) using the parameters in Table II, plotted as a function of perturber number density ρ_{P}. (a) P is Ar at (●, ○) −114.8 °C, at (■, □) −117.6 °C, and at (▲, △) various other noncritical temperatures. (b) P is Kr at (●, ○) −57.1 °C, at (■, □) −60.0 °C, and at (▲, △) various other noncritical temperatures. Solid markers represent D=$\mathrm{CH_3I}$, and open markers represent D=$\mathrm{C_2H_5I}$. The lines are a nonlinear least-squares fit to experiment using a seventh-order polynomial function and are provided as a visual aid. See text for discussion.

Under these boundary conditions, Eq. (43) has the solution [cf. Eq. (28)]

$$\psi_0 = \frac{1}{r}\sin k_0(r - |A|), \tag{45}$$

where [cf. Eq. (29)]

$$\tan k_0(r_\ell - |A|) = k_0 r_\ell. \tag{46}$$

In Eq. (46), the phase shift due to s-wave scattering from the hard-core potential that represents the central rare-gas atom is $-k_0|A|$ [75]. Outside the first solvent shell, however, the quasifree-electron wave function can also scatter off of the rare-gas atoms contained within the solvent shell, which introduces an additional phase shift. Again for s-wave scattering, and in the limit of small k_0, this scattering phase shift is given by $\eta\pi$, where η is the phase-shift amplitude [76]. Incorporating this phase shift into Eq. (46) yields

$$\tan[k_0(r_\ell - |A|) + \eta\pi] = k_0 r_\ell. \tag{47}$$

In this model, η is an adjustable parameter for each perturber and is evaluated from the field ionization and/or photoconduction data for $V_0(\rho_{\mathrm{P}})$. Once the thermal kinetic energy of the quasifree electron is included, $V_0(\rho_{\mathrm{P}})$ becomes

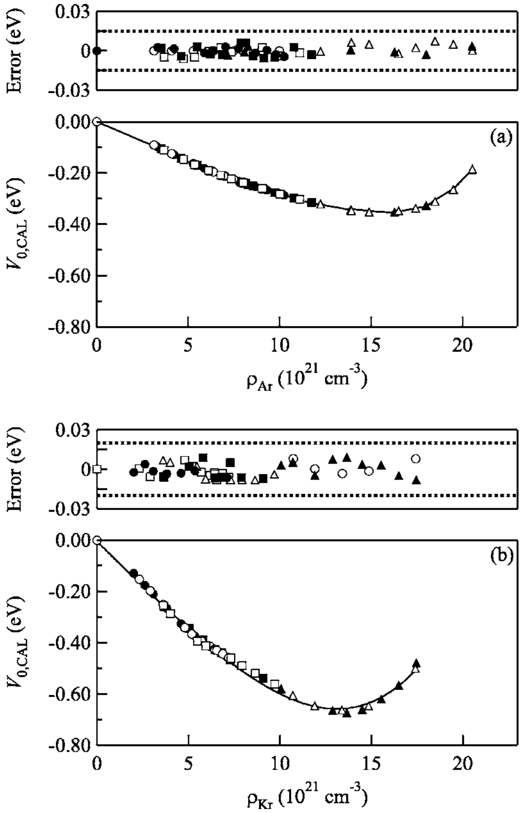

FIG. 10. $V_{0,\mathrm{CAL}}(\rho_{\mathrm{P}})$, calculated from Eq. (48), plotted as a function of perturber number density ρ_{P}. (a) P is Ar at (●, ○) −114.8 °C, at (■, □) −117.6 °C, and at (▲, △) various other noncritical temperatures. (b) P is Kr at (●, ○) −57.1 °C, at (■, □) −60.0 °C, and at (▲, △) various other noncritical temperatures. Solid markers represent D=CH_3I, and open markers represent D=C_2H_5I. (—) is a nonlinear least-squares fit to the experimental data of Fig. 8 using $V_{0,\mathrm{EXP}}(\rho_{\mathrm{P}})=a_0+a_1(\rho_{\mathrm{P}}-a_2)+(a_3/a_4)\ln\{\cosh[a_4(\rho_{\mathrm{P}}-a_2)]\}$ [1,6]. The error shown is the difference between the experimental $V_0(\rho_{\mathrm{P}})$ in Fig. 8 and the calculated values. The horizontal dotted lines represent the experimental error limits. See text for discussion.

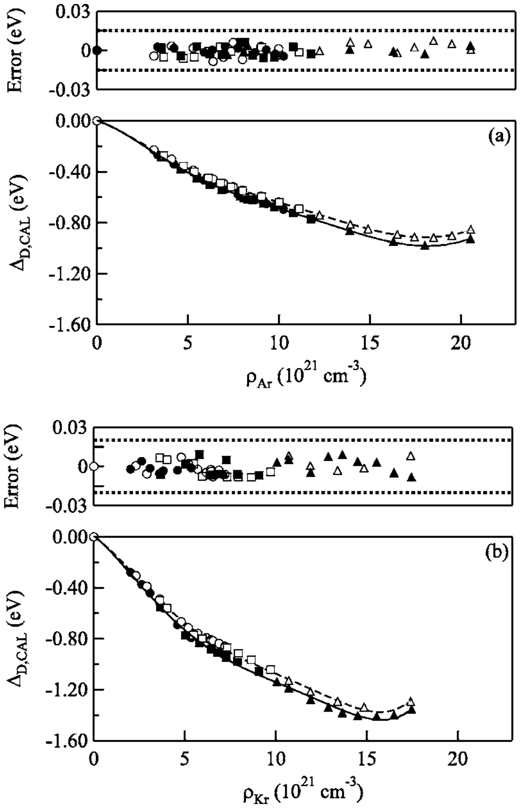

FIG. 11. $\Delta_{\mathrm{D,CAL}}(\rho_{\mathrm{P}})$, calculated from Eq. (4) with $P_+(\rho_{\mathrm{P}})$ from Fig. 7 and $V_0(\rho_{\mathrm{P}})=V_{0,\mathrm{CAL}}(\rho_{\mathrm{P}})$ from Fig. 10, plotted as a function of perturber number density ρ_{P}. (a) P is Ar at (●, ○) −114.8 °C, at (■, □) −117.6 °C, and at (▲, △) various other noncritical temperatures. (b) P is Kr at (●, ○) −57.1 °C, at (■, □) −60.0 °C, and at (▲, △) various other noncritical temperatures. Solid markers represent D=CH_3I, and open markers represent D=C_2H_5I. Lines are nonlinear least-squares fits of the experimental data in Fig. 6 using a seventh-order polynomial function and are provided as a visual aid. The error shown is the difference between the experimental $\Delta_{\mathrm{D,EXP}}(\rho_{\mathrm{P}})$ in Fig. 6 and the calculated values. The horizontal dotted lines represent the experimental error limits. See text for discussion.

$$V_0(\rho_{\mathrm{P}}) = E_k(\rho_{\mathrm{P}}) + P_-(\rho_{\mathrm{P}}) + \frac{3}{2}k_BT,$$

$$E_k(\rho_{\mathrm{P}}) = \frac{(\hbar k_0)^2}{2m}, \tag{48}$$

where k_0 is evaluated from Eq. (47).

Figure 10(a) presents $V_{0,\mathrm{CAL}}(\rho_{\mathrm{P}})$ for Ar obtained from Eq. (48) with $\eta=0.40$ and $A=-0.82$ Å [21], plotted as a function of Ar number density ρ_{Ar}. Similarly, Fig. 10(b) presents $V_{0,\mathrm{CAL}}(\rho_{\mathrm{P}})$ for Kr calculated with $\eta=0.48$ and $A=-1.60$ Å [21], plotted as a function of krypton number density ρ_{Kr}. The solid line in Fig. 10 is a nonlinear least-squares fit of the experimental data from Fig. 8 using an empirical function from [1]. The error shown at the top of both Figs. 10(a) and 10(b) is the difference between the experimentally determined $V_0(\rho_{\mathrm{P}})$ values (cf. Fig. 8) and the values calculated from Eq. (48), represented by the individual markers. The horizontal dotted lines denote the overall experimental error limits. Clearly, the error between the calculated and experimental $V_0(\rho_{\mathrm{P}})$ values falls within the intrinsic error of these measurements. It is important to note that the only adjustable parameter in this model is η, which is perturber-dependent. Finally, Fig. 11 shows the total perturber-induced shift of dopant ionization energy $\Delta_{\mathrm{D}}(\rho_{\mathrm{P}})$ for both dopants (CH_3I and C_2H_5I) in both perturbers (Ar and Kr). The solid (CH_3I) and dashed (C_2H_5I) lines provide a nonlinear least-squares fit to the experimental data as a visual aid, and the error between the calculated and experimental values is provided at the top of both Figs. 11(a) (Ar) and 11(b) (Kr). Again, the differences between the experimental and calculated values fall well within the experimental error limits.

Finally, as an additional test of the model leading to Eq. (48), we have calculated $V_0(\rho_{\mathrm{P}})$ for Xe. The Lennard-Jones parameters used in the radial distribution function and polarization shift calculations are $\sigma_{\text{Xe-Xe}}=4.10$ Å and $\varepsilon_{\text{Xe-Xe}}/k_B=221.0$ K. Figure 12 presents a collection of published mea-

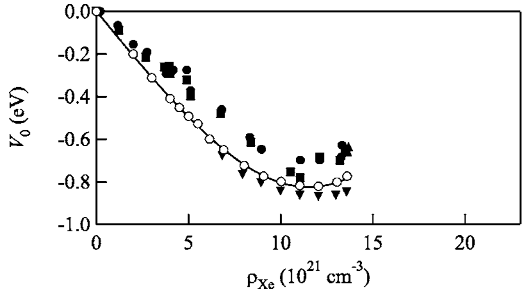

FIG. 12. $V_0(\rho_P)$ for Xe plotted as a function of xenon number density (ρ_{Xe}). (●) [3], (■) [3], and (▲) [11] are from photoinjection measurements. (▼) is from Eq. (4) with $\Delta_D(\rho_P)$ obtained from the field ionization of $(CH_3)_2S$ in Xe, and $P_+(\rho_P)$ calculated using Eq. (13) [32]. (○) is $V_{0,CAL}(\rho_P)$ for Xe determined from Eq. (48) with $\eta=0.50$. (—) is a nonlinear least-squares fit to $V_{0,calc}(\rho_P)$ using an empirical equation from [1] and is provided as a visual aid.

surements (solid markers) of $V_0(\rho_P)$ for Xe, plotted as a function of number density ρ_{Xe}, and compares these to our calculated values (open markers and solid line) obtained from Eq. (48) with $\eta=0.50$ and $A=-3.24$ Å [21]. The model calculation clearly falls within the scatter of the experimental points. However, a more comprehensive Xe experimental data set is needed to explore fully the accuracy of $V_0(\rho_P)$ calculated using this new model.

The new local Wigner-Seitz model presented here provides $V_0(\rho_P)$ calculations to within ±0.1% of experiment for Ar and Kr, and falls within the scatter of the experimental points for Xe, with the use of only one adjustable parameter. This represents an order of magnitude improvement in accuracy in comparison to previously published $V_0(\rho_P)$ models.

VI. CONCLUSIONS

We have presented experimental data for $V_0(\rho_P)$ determined from field ionization of dopant (CH_3I and C_2H_5I) Rydberg states in dense Ar and Kr, along select isotherms that did not include the critical isotherm. We have shown that there is little to no temperature dependence in $V_0(\rho_P)$ along these noncritical isotherms. We have developed a new local Wigner-Seitz model that contains only one adjustable parameter and that allows one to fit the experimental data to within ±0.1%. This new model differs from the original SJC model by calculating the polarization energy using a statistical mechanical approach, by using a local Wigner-Seitz radius based upon the local number density instead of the bulk number density, by including the thermal energy of the electron, and by introducing a phase shift to represent the scattering of the quasifree electron off of the rare-gas atoms within the solvent shell. While this model was developed for Ar and Kr, we also showed that it reproduces the known $V_0(\rho_P)$ data for Xe. Future papers will describe the behavior of $V_0(\rho_P)$ along the critical isotherm near the critical density of Ar and Kr, as well as the application of the local Wigner-Seitz model to these near-critical point systems [70–72], and future work will focus on an extension of these techniques to molecular perturbers and a systematic assessment of the perturber dependence of the phase-shift parameter η.

ACKNOWLEDGMENTS

We are grateful to Dr. Ruben Reininger (University of Wisconsin Synchrotron Radiation Center) for many helpful discussions. We thank Luxi Li (Queens College) for her assistance in the error calculations contained in Figs. 10 and 11. The experimental measurements reported here were performed at the University of Wisconsin Synchrotron Radiation Center (NSF DMR-0084402). This work was supported by grants from the Louisiana Board of Regents Support Fund [LEQSF (1997-00)-RD-A-14], from the Petroleum Research Foundation (41378-G6), and from the Professional Staff Congress City University of New York (60073 - 34 35).

---

[1] S. Basak and M. H. Cohen, Phys. Rev. B **20**, 3404 (1979).
[2] Y. Yamaguchi, T. Nakajima, and M. Nishikawa, J. Chem. Phys. **71**, 550 (1979).
[3] R. Reininger, U. Asaf, and I. T. Steinberger, Chem. Phys. Lett. **90**, 287 (1982).
[4] K. Nakagawa, K. Ohtake, and M. Nishikawa, J. Electrost. **12**, 157 (1982).
[5] U. Asaf, R. Reininger, and I. T. Steinberg, Chem. Phys. Lett. **100**, 363 (1983).
[6] R. Reininger, U. Asaf, I. T. Steinberger, and S. Basak, Phys. Rev. B **28**, 4426 (1983).
[7] A. F. Borghesani, L. Bruschi, M. Santini, and G. Torzo, Phys. Rev. A **37**, 4828 (1988).
[8] A. F. Borghesani, M. Santini, and P. Lamp, Phys. Rev. A **46**, 7902 (1992).
[9] V. M. Atrazhev and I. T. Iakubov, J. Chem. Phys. **103**, 9930 (1995).
[10] A. F. Borghesani and M. Santini, Int. J. Thermophys. **22**, 1109 (2001).
[11] I. T. Steinberger, in *Classical Rare Gas Liquids*, edited by W. F. Schmidt and E. Illenberger (Am. Sci. Publ., in press), and references therein.
[12] M. Nishikawa, K. Itoh, and R. A. Holroyd, J. Phys. Chem. **92**, 5262 (1988).
[13] K. Itoh and R. A. Holroyd, J. Phys. Chem. **94**, 8854 (1990).
[14] E. Fermi, Nuovo Cimento **11**, 157 (1934).
[15] V. A. Alekseev and I. I. Sobel'man, Zh. Eksp. Teor. Fiz. **49**, 1274 (1965) [Sov. Phys. JETP **22**, 882 (1966)].
[16] I. I. Sobel'man, L. A. Vainshtein, and E. A. Yukov, *Excitation of Atoms and Broadening of Spectral Lines* (Springer-Verlag, Berlin, 1981).
[17] A. M. Köhler, Ph.D. dissertation, Universitat Hamburg (1987), and references therein.
[18] A. M. Köhler, V. Saile, R. Reininger, and G. L. Findley, Phys. Rev. Lett. **60**, 2727 (1988).
[19] A. M. Köhler, R. Reininger, V. Saile, and G. L. Findley, Phys.

Rev. A **33**, R771 (1986).

[20] A. M. Köhler, R. Reininger, V. Saile, and G. L. Findley, Phys. Rev. A **35**, 79 (1987).

[21] C. M. Evans, Ph.D. dissertation, Louisiana State University (2001), and references therein. See also C. M. Evans, J. D. Scott, and G. L. Findley, Rec. Res. Dev. Chem. Phys. **3**, 351 (2002).

[22] *Photophysics and Photochemistry in the Vacuum Ultraviolet*, edited by S. P. McGlynn, G. L. Findley, and R. H. Huebner (D. Reidel, Dordrecht, 1985), and references therein.

[23] J. Meyer, Ph.D. dissertation, Universitat Hamburg (1992), and references therein.

[24] A. K. Al-Omari, Ph.D. dissertation, University of Wisconsin Madison (1996), and references therein.

[25] B. Helpern, J. Lekner, S. A. Rice, and R. Gomer, Phys. Rev. **156**, 351 (1967).

[26] U. Asaf and I. T. Steinberger, Chem. Phys. Lett. **128**, 91 (1986).

[27] R. A. Holroyd and M. Allen, J. Chem. Phys. **54**, 5014 (1971).

[28] R. A. Holroyd and W. Tauchert, J. Chem. Phys. **60**, 3715 (1974).

[29] K. Nakagawa, K. Itoh, and M. Nishikawa, IEEE Trans. Electr. Insul. **23**, 509 (1988).

[30] W. Tauchert and W. F. Schmidt, Z. Naturforsch. A **30A**, 1095 (1975).

[31] A. K. Al-Omari, R. Reininger, and D. L. Huber, J. Chem. Phys. **109**, 7663 (1998).

[32] K. N. Altmann and R. Reininger, J. Chem. Phys. **107**, 1759 (1997).

[33] A. K. Al-Omari, K. N. Altmann, and R. Reininger, J. Chem. Phys. **105**, 1305 (1996).

[34] A. K. Al-Omari and R. Reininger, J. Electron Spectrosc. Relat. Phenom. **79**, 463 (1996).

[35] A. K. Al-Omari and R. Reininger, J. Chem. Phys. **103**, 4484 (1995).

[36] A. K. Al-Omari and R. Reininger, J. Chem. Phys. **103**, 506 (1995).

[37] A. K. Al-Omari, R. Reininger, and D. L. Huber, Phys. Rev. Lett. **74**, 820 (1995).

[38] J. Meyer and R. Reininger, Phys. Rev. A **47**, R3491 (1993).

[39] T. F. Gallagher, *Rydberg Atoms* (Cambridge Univ. Press, Cambridge, 1994), and references therein.

[40] J. Lekner, Phys. Rev. **158**, 130 (1967).

[41] I. Messing, B. Raz, and J. Jortner, J. Chem. Phys. **66**, 4577 (1977).

[42] I. Messing, B. Raz, and J. Jortner, J. Chem. Phys. **66**, 2239 (1977).

[43] E. W. Grundke, D. Henderson, and R. D. Murphy, Can. J. Phys. **51**, 1216 (1973).

[44] B. E. Springett, J. Jortner, and M. H. Cohen, J. Chem. Phys. **48**, 2720 (1968).

[45] Y. Frongillo, B. Plenkiewicz, and J. P. Jay-Gerin, Phys. Rev. E **53**, 5506 (1996).

[46] B. Plenkiewicz, J. P. Jay-Gerin, P. Plenkiewicz, and G. B. Bachelet, Europhys. Lett. **1**, 455 (1986).

[47] B. Plenkiewicz, P. Plenkiewicz, J. P. Jay-Gerin, and A. K. Jain, J. Chem. Phys. **90**, 4907 (1989).

[48] B. Plenkiewicz, P. Plenkiwicz, and J. P. Jay-Gerin, Chem. Phys. Lett. **163**, 542 (1989).

[49] B. Plenkiewicz, P. Plenkiewicz, and J. P. Jay-Gerin, Phys. Rev. A **39**, 2070 (1989).

[50] B. Plenkiewicz, P. Plenkiewicz, and J. P. Jay-Gerin, Phys. Rev. A **40**, 4113 (1989).

[51] P. Stampfli and K. H. Bennemann, Phys. Rev. A **44**, 8210 (1991).

[52] E. Wigner and F. Seitz, Phys. Rev. **43**, 804 (1933).

[53] E. Wigner and F. Seitz, Phys. Rev. **46**, 509 (1934).

[54] B. Plenkiewicz, Y. Frongillo, P. Plenkiewicz, and J. P. Jay-Gerin, Phys. Rev. A **43**, 7061 (1991).

[55] I. T. Iakubov and V. V. Pogosov, Phys. Rev. B **51**, 14941 (1995).

[56] B. Boltjes, C. de Graff, R. P. H. Rettschnick, and S. W. de Leeuw, J. Chem. Phys. **97**, 408 (1992).

[57] B. Boltjes, C. de Graaf, and S. W. de Leeuw, J. Chem. Phys. **98**, 592 (1993).

[58] J. M. Lopez-Castillo, Y. Frongillo, B. Plenkiewicz, and J. P. Jay-Gerin, J. Chem. Phys. **96**, 9092 (1992).

[59] S. H. Simon, V. Dobrosavljevic, and R. M. Stratt, Phys. Rev. A **42**, R6278 (1990).

[60] S. H. Simon, V. Dobrosavljevic, and R. M. Stratt, J. Chem. Phys. **94**, 7360 (1991).

[61] B. Space, D. F. Coker, Z. H. Liu, B. J. Berne, and G. Martyna, J. Chem. Phys. **97**, 2002 (1992).

[62] J. M. Lopez-Castillo and J. P. Jay-Gerin, Phys. Rev. E **52**, 4892 (1995).

[63] T. R. Strobridge, Tech. Note 129, Nat. Bur. Std. (U.S.) (1962).

[64] A. L. Gosman, R. D. McCarty, and J. G. Hust, Tech. Note 27, Nat. Bur. Std. (U.S.) (1969).

[65] W. B. Streett and L. A. K. Staveley, J. Chem. Phys. **55**, 2495 (1971).

[66] J. O. Hireschfelder, C. F. Curtiss, and R. B. Bird, *Molecular Theory of Gases and Liquids* (Wiley, New York, 1954).

[67] P. T. Sikora, J. Phys. B **3**, 1475 (1970).

[68] J. M. Caillo, J. Chem. Phys. **109**, 4885 (1998).

[69] J. J. Potoff and A. Z. Panagiotopoulos, J. Chem. Phys. **109**, 10914 (1998).

[70] C. M. Evans and G. L. Findley, Chem. Phys. Lett. **410**, 242 (2005).

[71] C. M. Evans and G. L. Findley J. Phys. B **38**, L269 (2005).

[72] C. M. Evans and G. L. Findley J. Phys. Chem. A (unpublished).

[73] P. Attard, J. Chem. Phys. **91**, 3072 (1989).

[74] P. Attard, J. Chem. Phys. **91**, 3083 (1989).

[75] N. F. Mott and H. S. W. Massey, *The Theory of Atomic Collisions* (Oxford Univ. Press, Oxford, 1965).

[76] F. Calogero, *Variable Phase Approach to Potential Scattering* (Academic Press, New York, 1967).